# Unidirectional Spatial and Spectral Smoothed Tensor Ring Decomposition for Hyperspectral Image Denoising and Destriping

Yang Zhou, Yong Chen, Jinshan Zeng, *Member, IEEE*, Wei He, *Senior Member, IEEE*, and Min Huang

***Abstract*— In this letter, we propose a novel unidirectional spatial and spectral smoothed tensor ring (U3STR) decomposition for hyperspectral image (HSI) denoising and destriping. The powerful tensor ring (TR) decomposition is introduced to explore the global spatial–spectral correlation of HSI, which transforms the restoration of HSI into estimating three TR factors. To address the local spatial–spectral smoothness of HSI and the directional characteristic of stripe noise, unidirectional spatial and spectral smoothed constraints are applied to the horizontal spatial and spectral TR factors, respectively. Moreover, considering that the stripe noise shares spatial correlation and local smoothness with the image component, we strategically utilize band-by-band low rank and unidirectional total variation (TV) regularization, effectively disentangling stripe noise from the image content without conflicting the image regularization. The proposed U3STR model is solved by the alternating direction method of multipliers (ADMM) algorithm effectively. Experimental results demonstrate that our method outperforms other HSI restoration methods in denoising and destriping, notably enhancing the quality of the restored image by an average of 3 dB over existing methods.**

***Index Terms*— Denoising, destriping, hyperspectral image (HSI), tensor ring (TR) decomposition.**

## I. Introduction

A HYPERSPECTRAL image (HSI) contains abundant spatial and spectral information, which is widely applied in various fields, such as building extraction [1] and ground object classification [2]. However, due to sensor malfunctions, atmospheric interference, and ground surface influences, the acquired HSI is inevitably degraded by Gaussian, impulse, and stripe noise, which greatly reduce the utility rate of HSI data. Therefore, HSI denoising has become an essential preprocessing step for subsequent applications.

In recent years, numerous HSI denoising methods have been developed, which can be roughly divided into two categories: deep learning (DL)-based approaches and model-based approaches. Owing to the potent nonlinear learning ability of deep neural networks, DL-based methods have been raised for HSI denoising. The main idea of such methods is to learn the mapping function from noisy HSI to potential clean HSI by various parameterized neural networks, such as convolutional neural networks [3] and Transformer networks [4]. Despite their effects in scenarios mirroring their training datasets, these methods often exhibit limitations in generalization ability, especially under diverse real-world conditions with varying Gaussian noise intensities and stripe noise proportions.

Model-based approaches treat HSI denoising as an ill-posed inverse problem, delving into statistical priors pertinent to the target imagery. The commonly used prior information in the HSI denoising task includes low rank, local smoothness, and nonlocal self-similarity. Low-rank prior is based on the global spatial–spectral correlation of HSI and primarily characterized by three types of tools: matrix nuclear norm, low-rank matrix factorization, and low-rank tensor factorization [5], [6], [7], [8], [9], [10], [11]. The performance of low-rank methods can be further improved by incorporating local spatial–spectral smoothness priors. Since the local regions and adjacent bands of HSI contain similar objects, the local smoothness prior usually exists within the spatial–spectral dimensions. Total variation (TV) regularization serves as an effective tool to encode the local smoothness prior. By incorporating the TV or enhanced TV regularization into the low-rank framework, a series of HSI denoising methods are developed [12], [13], [14], [15]. Given the prevalence of similar patterns within the spatial dimension of HSI, nonlocal self-similarity prior is frequently used for HSI denoising and has achieved advanced performances [16], [17], [18]. Despite rapid advancements in HSI denoising, the above methods struggle under complex mixed noise conditions, especially high-level stripe noise.

Recently, in response to the complex mixed noise with high-level stripe noise, joint HSI denoising and destriping methods have emerged. These methods treat the stripe noise as an independent component rather than as sparse noise, while simultaneously considering the prior information of both the image component and the stripe noise. For example, Zhang et al. [19] and Su et al. [20] proposed a double low-rank (DLR) matrix decomposition method and a fast graph Lapla-

Manuscript received 5 April 2024; revised 24 May 2024; accepted 6 June 2024. Date of publication 11 June 2024; date of current version 19 June 2024. This work was supported in part by the National Natural Science Foundation of China under Grant 62101222, Grant 42201438, and Grant 62376110; in part by the Natural Science Foundation of Jiangxi, China, under Grant 20232ACB212001, Grant 20224BAB212001, and Grant 20224ACB212004; and in part by the Young Elite Scientists Sponsorship Program by Jiangxi Association for Science and Technology (JXAST) under Grant 2023QT12. *(Corresponding author: Yong Chen.)*

Yang Zhou, Yong Chen, and Jinshan Zeng are with the School of Computer and Information Engineering, Jiangxi Normal University, Nanchang 330022, China (e-mail: 202126204017@jxnu.edu.cn; chenyong1872008@163.com; jinshanzeng@jxnu.edu.cn).

Wei He is with the State Key Laboratory of Information Engineering in Surveying, Mapping and Remote Sensing, Wuhan University, Wuhan 430072, China (e-mail: weihe1990@whu.edu.cn).

Min Huang is with the School of Geography and Environment, Jiangxi Normal University, Nanchang 330022, China (e-mail: huangm@jxnu.edu.cn).

This article has supplementary downloadable material available at https://doi.org/10.1109/LGRS.2024.3412804, provided by the authors.

Digital Object Identifier 10.1109/LGRS.2024.3412804

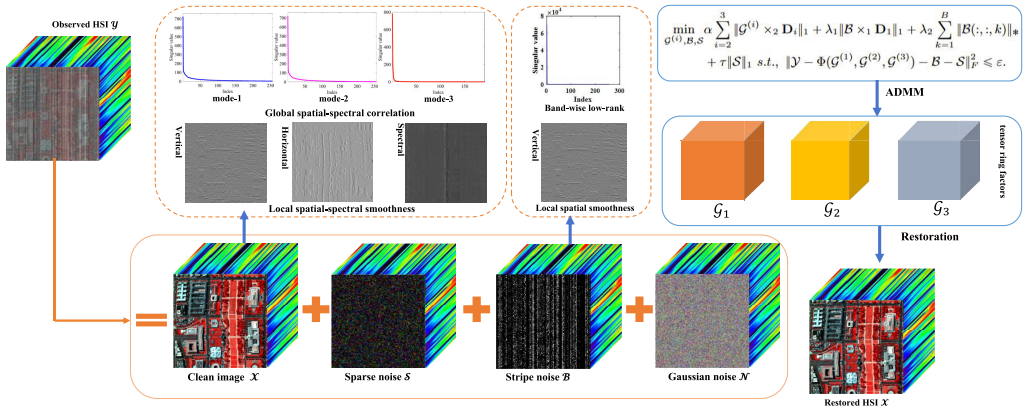


Fig. 1. Framework of the proposed U3STR. The TR decomposition and unidirectional spatial and spectral TV regularization are designed to capture the global spatial–spectral correlation and local spatial–spectral smoothness of HSI. Moreover, band-by-band low rank and unidirectional spatial TV regularizations are employed to estimate the stripe noise.

cian regularizer (FGLR) for HSI denoising and destriping, respectively. However, the majority of the existing methods are based on matrix modeling to depict the prior information of HSI, which inevitably disrupts the spatial structure of HSI. Considering the intrinsic 3-D structure of HSI, tensor-based modeling could more effectively capture and retain the spatial–spectral information of HSI.

In this letter, we propose a novel unidirectional spatial and spectral smoothed tensor ring (U3STR) decomposition for HSI denoising and destriping, effectively eliminating the dense stripe noise in mixed noise scenarios (see Fig. 1). The main contributions of this letter are delineated as follows.

1) To effectively preserve the spatial–spectral correlation of HSI, a novel tensor ring (TR) decomposition is designed to approximate the HSI, which transforms the restoration into estimating three TR factors. Moreover, we employ unidirectional spatial and spectral smoothed regularizations to constrain the spatial horizontal and spectral TR factors, respectively, instead of directly regularizing the HSI itself to explore the local smooth characteristic.
2) To discriminatively separate the dense stripe noise from the image, the band-by-band low rank and unidirectional TV regularization terms are employed to constrain the stripe noise, which avoid conflict with the image component. Experimental results substantiate that our method outperforms the existing HSI restoration methods.

## II. Notations and Preliminaries

### A. Notations

Scalar, vector, matrix, and tensor are denoted by $x$, $\mathbf{x}$, $\mathbf{X}$, and $\mathcal{X}$, respectively. For an $n$-way tensor $\mathcal{X} \in \mathbb{R}^{I_1 \times I_2 \times \cdots \times I_n}$, $\mathbf{X}_{(k)} \in \mathbb{R}^{I_k \times I_1, \ldots, I_{k-1} I_{k+1}, \ldots, I_n}$ and $\mathbf{X}_{\langle k \rangle} \in \mathbb{R}^{I_k \times I_{k+1}, \ldots, I_n I_1, \ldots, I_{k-1}}$ denote the first mode-$k$ and second mode-$k$ unfolding matrices of $\mathcal{X}$, respectively. We use $\mathcal{X}(i,:,:)$, $\mathcal{X}(:,j,:)$, and $\mathcal{X}(:,:,k)$ to denote, respectively, the $i$th horizontal, $j$-lateral, and $k$-frontal slice of a three-way tensor $\mathcal{X} \in \mathbb{R}^{I_1 \times I_2 \times I_3}$, respectively. The $\ell_1$ norm and Frobenius norm are defined‘ as $\|\mathcal{X}\|_1 = \sum_{i_1 i_2, \ldots, i_n} |x_{i_1 i_2, \ldots, i_n}|$ and $\|\mathcal{X}\|_F = (\sum_{i_1 i_2, \ldots, i_n} |x_{i_1 i_2, \ldots, i_n}|^2)^{1/2}$, respectively. The matrix nuclear norm is defined as $\|\mathbf{X}\|_* = \sum_i \sigma_i(\mathbf{X})$, where $\sigma_i(\mathbf{X})$ is the $i$th singular value of $\mathbf{X}$. The mode-$k$ tensor–matrix product of a tensor $\mathcal{X} \in \mathbb{R}^{I_1 \times I_2 \times \cdots \times I_n}$ and a matrix $\mathbf{U} \in \mathbb{R}^{J \times I_k}$ is an $I_1 \times I_2 \times \cdots \times I_{k-1} \times J \times I_{k+1} \cdots \times I_n$ tensor denoted by $\mathcal{X} \times_k \mathbf{U}$ and satisfied $(\mathcal{X} \times_k \mathbf{U})_{i_1, \ldots, i_{k-1} j i_{k+1}, \ldots, i_n} = \sum_{i_k=1}^{I_k} x_{i_1 i_2, \ldots, i_n} u_{j i_k}$.

### B. Preliminaries

TR decomposition represents that an $n$-way tensor $\mathcal{X} \in \mathbb{R}^{I_1 \times I_2 \times \cdots \times I_n}$ is decomposed as a series of three-way tensor factors $\mathcal{G}^{(1)}$, $\mathcal{G}^{(2)}, \ldots,$ and $\mathcal{G}^{(n)}$, where $\mathcal{G}^{(k)} \in \mathbb{R}^{r_k \times I_k \times r_{k+1}}$ and $r_1 = r_{n+1}$. $r = [r_1, r_2, \ldots, r_n]$ is denoted as TR rank [21]. Mathematically, it is formulated as follows:

$$\mathcal{X} = \Phi(\mathcal{G}^{(1)}, \mathcal{G}^{(2)}, \ldots, \mathcal{G}^{(n)}) \tag{1}$$

where $\mathcal{X}_{i_1 i_2, \ldots, i_n} = \mathbf{Trace}(\mathbf{G}_{(i_1)}^{(1)} \mathbf{G}_{(i_2)}^{(2)}, \ldots, \mathbf{G}_{(i_n)}^{(n)})$, $\mathcal{G}_{i_k}^{k}$ denotes the $i_k$-th lateral slice matrix of $\mathcal{G}^{(k)}$, and Trace$(\cdot)$ is the matrix trace operation. The tensor multilinear product of two adjacent tensor factors $\mathcal{G}^{(k)} \in \mathbb{R}^{r_k \times I_k \times r_{k+1}}$ and $\mathcal{G}^{(k+1)} \in \mathbb{R}^{r_{k+1} \times I_{k+1} \times r_{k+2}}$ is defined as follows:

$$\mathcal{G}^{(k,k+1)}((j_k - 1) I_n + i_k) = \mathcal{G}^{(k)}(i_k) \mathcal{G}^{(k+1)}(j_k) \tag{2}$$

for $i_k = 1, \ldots, I_k$, $j_k = 1, \ldots, I_{k+1}$, and where $\mathcal{G}^{(k,k+1)} \in \mathbb{R}^{r_k \times I_k I_{k+1} \times r_{k+2}}$. The matrix representation of TR decomposition is formulated as follows:

$$\mathbf{X}_{\langle k \rangle} = \mathbf{G}_{\langle 2 \rangle}^{(k)} \left( \mathbf{G}_{\langle 2 \rangle}^{(\neq k)} \right)^T, \quad (k = 1, \ldots, n) \tag{3}$$

where $\mathbf{G}_{\langle 2 \rangle}^{(\neq k)}$ is the matrix unfolding of $\mathcal{G}^{(k+1, k+2, \ldots, n, 1, \ldots, k-1)} \in \mathbb{R}^{r_{k+1} \times \prod_{i=1, i \neq k}^{n} I_i \times r_k}$.

## III. Proposed Method

### A. Problem Formulation

We assume that the observed HSI is degraded by mixed noise, including Gaussian noise, impulse noise, and stripe noise. To address the high-intensity stripe noise in practical scenarios, we formulate the HSI degradation model as follows:

$$\mathcal{Y} = \mathcal{X} + \mathcal{B} + \mathcal{S} + \mathcal{N} \tag{4}$$

where $\mathcal{Y}$, $\mathcal{X}$, $\mathcal{B}$, $\mathcal{S}$, and $\mathcal{N}$ denote the observed HSI, clean HSI, stripe noise, sparse noise (impulse noise), and Gaussian noise, respectively. All entities are the dimension of $M \times N \times B$, where $M \times N$ denotes the spatial dimension and $B$ denotes the spectral dimension.

The task of restoring $\mathcal{X}$ from $\mathcal{Y}$ is an ill-posed inverse problem, and the regularization model can be formulated as follows:

$$\min_{\mathcal{X},\mathcal{B},\mathcal{S}} \alpha R_{\mathcal{X}}(\mathcal{X}) + \lambda R_{\mathcal{B}}(\mathcal{B}) + \tau R_{\mathcal{S}}(\mathcal{S}) \quad \text{s.t. } \|\mathcal{Y} - \mathcal{X} - \mathcal{B} - \mathcal{S}\|_F^2 \le \varepsilon \tag{5}$$

where $R_{\mathcal{X}}(\mathcal{X})$, $R_{\mathcal{B}}(\mathcal{B})$, and $R_{\mathcal{S}}(\mathcal{S})$ serve as the regularization terms describing the prior information of the desired HSI, stripe noise, and sparse noise, respectively. $\alpha$, $\lambda$, and $\tau$ are regularization parameters, and $\varepsilon$ represents the level of Gaussian noise. For sparse noise $\mathcal{S}$, $R_{\mathcal{S}}(\mathcal{S})$ is typically set as $\|\mathcal{S}\|_1$.

### B. Proposed U3STR Model

*1) Prior Information of HSI:* From Fig. 1, it can be observed that the HSI exhibits a high correlation in the spatial–spectral dimension. To capture the spatial–spectral correlation, traditional Tucker decomposition and CANDECOMP/PARAFAC (CP) decomposition can be employed to approximate the HSI. However, Tucker decomposition is limited by a rapid increase in parameter numbers due to its core tensor, while CP decomposition simplistically assumes equal importance of spatial and spectral correlations, overlooking the generally higher spectral correlation within HSI. Recently, TR decomposition has emerged as superior to both Tucker and CP in handling various HSI tasks, such as HSI completion [22] and fusion [23], with its benefits including the following: 1) a significantly reduced parameter count compared with Tucker decomposition and 2) TR factors can be circularly shifted and treated equivalently, enabling a balanced consideration of all dimensional correlations. Therefore, we employ the TR decomposition to approximate the HSI, i.e.,

$$\mathcal{X} = \Phi(\mathcal{G}^{(1)}, \mathcal{G}^{(2)}, \mathcal{G}^{(3)}) \tag{6}$$

where $\mathcal{G}^{(1)}$ and $\mathcal{G}^{(2)}$ are two spatial TR factors in the spatial vertical dimension and spatial horizontal dimension, respectively, and $\mathcal{G}^{(3)}$ is the spectral TR factor.

In addition to the global spatial–spectral correlation, HSI also has local spatial–spectral smoothness. To capture this prior information, exploring the interplay between HSI and its TR factors is crucial. From the matrix representation of TR decomposition in (3), it is clear that all columns of $\mathbf{G}_{(2)}^{(k)}$ form the basis set for the lower dimensional space of $\mathbf{X}_{\langle k \rangle}$. Based on the principle that continuous basis can generate continuous data, the local smoothness constraint of each column of the factor $\mathbf{G}_{(2)}^{(k)}$ can maintain the local smoothness of HSI in the mode-$k$ dimension. Considering that stripe noise presents stronger local smoothness in the spatial vertical dimension, we consequently employ the unidirectional spatial and spectral smoothed regularizations to constrain the spatial horizontal and spectral TR factors, respectively, i.e.,

$$R_{\mathbf{smooth}}(\mathcal{X}) = \|\mathcal{G}^{(2)} \times_2 \mathbf{D}_2\|_1 + \|\mathcal{G}^{(3)} \times_2 \mathbf{D}_3\|_1 \tag{7}$$

where $\mathbf{D}_2 \in \mathbb{R}^{N\times N}$ and $\mathbf{D}_3 \in \mathbb{R}^{B\times B}$ are first-order difference matrices.

*2) Prior Information of Stripe Noise:* Unlike other noise, stripe noise exhibits significant structural characteristics. Compared with the image component, stripe noise is not only more low rank in the spatial vertical dimension but also shows greater local smoothness along the stripe direction. To depict the structural properties of stripe noise and avoid conflicts with image regularizations, we formulate $R_{\mathcal{B}}$ as follows:

$$R_{\mathcal{B}}(\mathcal{B}) = \lambda_1 \|\mathcal{B} \times_1 \mathbf{D}_1\|_1 + \lambda_2 \sum_{k=1}^{B} \|\mathcal{B}(:,:,k)\|_* \tag{8}$$

where $\mathbf{D}_1 \in \mathbb{R}^{M\times M}$ is the first-order difference matrix.

Based on the above prior exploration and regularization term design, the proposed U3STR model is formulated as follows:

$$\min_{\mathcal{G}^{(i)},\mathcal{B},\mathcal{S}} \alpha \sum_{i=2}^{3} \|\mathcal{G}^{(i)} \times_2 \mathbf{D}_i\|_1 + \lambda_1 \|\mathcal{B} \times_1 \mathbf{D}_1\|_1 + \lambda_2 \sum_{k=1}^{B} \|\mathcal{B}(:,:,k)\|_* + \tau \|\mathcal{S}\|_1 \quad \text{s.t. } \|\mathcal{Y} - \Phi(\mathcal{G}^{(1)}, \mathcal{G}^{(2)}, \mathcal{G}^{(3)}) - \mathcal{B} - \mathcal{S}\|_F^2 \le \varepsilon. \tag{9}$$

Model (9) can be solved by alternating direction method of multipliers (ADMM) [24] effectively. A detailed optimization process can be found in the supplementary material.

## IV. Experimental Results

In this section, we conduct experiments on both simulated and real data to substantiate the effectiveness of the proposed method. Six HSI denoising and destriping methods are chosen for comparison, including low-rank tensor decomposition method (LRTD) [6], fast and parameter-free HSI mixed noise removal method (FastHyMix) [8], adaptive HSI mixed noise removal method (Adhyde) [18], bandwise asymmetric Laplacian noise-based matrix factorization method (BALMF) [9], DLR [19], and FGLR [20]. The peak signal-to-noise ratio (PSNR), structural similarity (SSIM), and spectral angle mapper (SAM) are employed to evaluate the restoration performance. We carefully fine-tuned the parameters according to the recommendations in the corresponding literature to ensure optimal performance in all tests. All experiments are implemented on MATLAB (R2021b) using Windows 11 with an Intel Core i7-8700 CPU 3.20-GHz processor and 16-GB RAM. The pixel values of each band are normalized to [0, 1].

### A. Simulated Experiments

Two HSI datasets, including Pavia City Center (Pavia) and Washington DC Mall (WDC), are employed as simulated datasets. The subimage sizes of Pavia and WDC are $200 \times 200 \times 80$ and $256 \times 256 \times 191$ in our simulated experiments, respectively. To comprehensively simulate a realistic mixed noisy HSI with high-intensity stripe noise, we consider the random stripe and periodic stripe that appeared in push-broom and cross-track scanning sensors, respectively. The simulated noise cases are presented as follows.

*Case 1:* Zero-mean Gaussian noise and impulse noise are added to all bands with different levels. The noise standard deviation of Gaussian noise and the percentage of impulse

TABLE I
QUANTITATIVE EVALUATION INDICES OF DIFFERENT METHODS ON THE SIMULATED PAVIA AND WDC DATASETS

| Dataset | Method | Case 1-1 | | | | Case 1-2 | | | | Case 2-1 | | | | Case 2-2 | | | |
|---|---|---|---|---|---|---|---|---|---|---|---|---|---|---|---|---|---|
| | | PSNR | SSIM | SAM | Time | PSNR | SSIM | SAM | Time | PSNR | SSIM | SAM | Time | PSNR | SSIM | SAM | Time |
| Pavia | LRTD | 15.04 | 0.260 | 40.02 | 23.3 | 15.25 | 0.276 | 39.68 | 29.7 | 14.95 | 0.251 | 40.31 | 31.0 | 15.04 | 0.251 | 40.08 | 36.3 |
| | FastHyMix | 31.66 | 0.933 | 10.28 | **0.1** | 30.30 | 0.909 | 10.56 | **0.1** | 26.06 | 0.693 | 43.99 | **0.1** | 22.76 | 0.583 | 47.92 | **0.2** |
| | Adhyde | 34.65 | **0.951** | **5.72** | 122.7 | 34.27 | **0.949** | 7.25 | 152.2 | 30.34 | 0.761 | 38.67 | 220.4 | 26.76 | 0.714 | 35.24 | 222.2 |
| | BALMF | 31.09 | 0.921 | 8.08 | 22.3 | 31.18 | 0.917 | 8.19 | 22.3 | 24.36 | 0.712 | 38.60 | 22.6 | 24.20 | 0.701 | 33.56 | 22.5 |
| | DLR | 32.95 | 0.934 | 7.36 | 13.0 | 32.95 | 0.934 | 7.06 | 13.5 | 33.59 | 0.947 | 6.89 | 15.0 | 32.24 | 0.925 | 7.41 | 15.0 |
| | FGLR | 32.03 | 0.928 | 7.38 | 1.5 | 31.81 | 0.926 | 8.31 | 1.5 | 31.17 | 0.924 | 9.04 | 1.0 | 31.81 | 0.926 | 10.76 | 1.1 |
| | U3STR | **34.90** | 0.943 | 6.17 | 18.4 | **34.60** | 0.942 | **6.23** | 18.1 | **35.81** | **0.954** | **5.64** | 18.1 | **33.89** | **0.934** | **6.48** | 18.8 |
| WDC | LRTD | 14.39 | 0.250 | 43.76 | 95.6 | 14.87 | 0.267 | 43.49 | 126.4 | 14.98 | 0.273 | 42.83 | 138.3 | 14.50 | 0.254 | 43.71 | 183.1 |
| | FastHyMix | 24.15 | 0.769 | 21.93 | **0.3** | 25.84 | 0.761 | 21.78 | **0.2** | 20.51 | 0.505 | 48.39 | **0.2** | 18.57 | 0.453 | 45.93 | **0.2** |
| | Adhyde | 35.02 | 0.946 | 7.01 | 244.4 | 35.50 | 0.954 | 7.58 | 226.9 | 29.98 | 0.755 | 38.09 | 365.7 | 29.11 | 0.721 | 36.55 | 452.7 |
| | BALMF | 32.66 | 0.942 | 8.26 | 71.3 | 33.11 | 0.945 | 8.36 | 84.0 | 22.06 | 0.617 | 44.42 | 84.3 | 21.51 | 0.580 | 41.41 | 83.9 |
| | DLR | 34.84 | 0.959 | 7.22 | 56.8 | 35.40 | **0.967** | 6.82 | 55.7 | 34.30 | **0.959** | 7.97 | 61.6 | 34.24 | **0.960** | **7.90** | 64.4 |
| | FGLR | 29.94 | 0.889 | 11.91 | 3.6 | 30.31 | 0.896 | 11.97 | 3.9 | 28.30 | 0.846 | 16.62 | 3.8 | 27.87 | 0.841 | 17.26 | 3.9 |
| | U3STR | **35.87** | **0.960** | **6.43** | 119.7 | **36.28** | 0.965 | **6.42** | 119.4 | **35.23** | 0.958 | **6.93** | 120.0 | **34.60** | 0.952 | 9.21 | 120.3 |

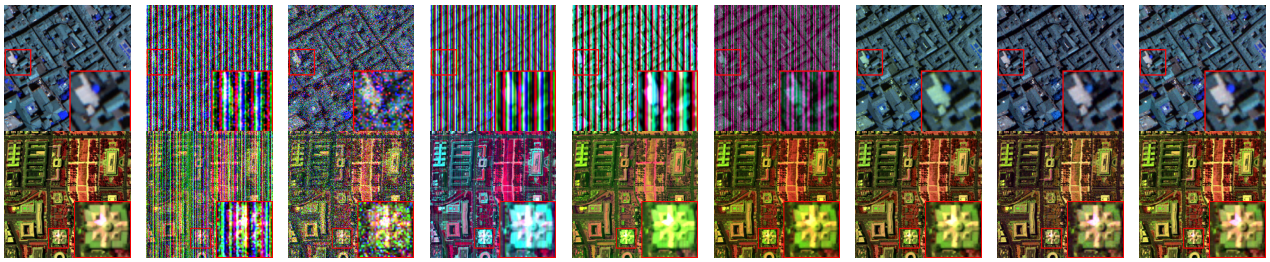


Fig. 2. (Top) Restored results of different methods on band (15, 48, 76) of the Pavia dataset under Case 2-1. (Bottom) Band (122, 48, 182) of the WDC dataset under Case 1-2.

noise in each band are randomly selected from the interval [0, 0.2]. Moreover, two different proportions of random stripe noise are added to the image: 1) 20%–30% and 2) 40%–50% of all bands are randomly selected to add stripes, and the number of stripes on each chosen band is randomly selected as follows: 1) 20%–30% and 2) 40%–50% of the image width.

*Case 2:* The Gaussian noise and impulse noise are added similar to Case 1. Moreover, the following hold: 1) 30% and 2) 50% of all bands are randomly selected to add periodic stripes, and the stripe proportion on each chosen band is set as follows: 1) 70% and 2) 50%. The period of stripes in each band is set as 10.

The quantitative metrics of different methods on the simulated experiments are listed in Table I, highlighting the best results for each index in bold. It is observed that the proposed U3STR outperforms the current state-of-the-art methods in terms of PSNR, SSIM, and SAM values in most cases. Moreover, the time cost is acceptable compared with other methods. To visually compare the restoration performance of different methods, false-color images of restoration results are presented in Fig. 2. The comparison methods FastHyMix, BALMF, and Adhyde model the noise as a nonindependent and identically distributed mixture of Gaussians (NMoG) modeling, effectively handling random stripes but struggling with periodic stripes. The U3STR method outperforms comparison methods in handling various mixed noise types, exceling in preserving spatial details and spectral consistency.

## B. Real Experiments

To further validate the performance of our U3STR, we test all methods on the real GaoFen-5 (GF-5) dataset, which is typically corrupted by a mixture of Gaussian noise, impulse noise, and dense stripe noise. A subregion of size $256 \times 256 \times 155$ is extracted for the experiment.

Visual comparison of denoising and destriping performance is conducted on a high-intensity noise band. Fig. 3 shows the restoration result on band 152 of the real GF-5 dataset. It can be observed that comparison methods exhibit some degree of excessive smoothness and spectral distortion, resulting in image detail loss. In contrast, U3STR effectively eliminates noise while preserving image detail.

TABLE II
AVERAGE QUANTITATIVE RESULTS OF ABLATION STUDIES ON THE PAVIA DATASET

| Method | w/o $\mathbf{D}_1$ | w/o $\mathbf{D}_2$ | w/o $\mathbf{D}_3$ | U3STR |
|---|---|---|---|---|
| PSNR | 34.39 | 34.08 | 32.30 | **34.80** |
| SSIM | 0.937 | 0.933 | 0.913 | **0.943** |
| SAM | 6.48 | 7.07 | 14.64 | **6.13** |

## C. Discussion

*1) Ablation Study:* To demonstrate the effectiveness of three distinct difference operator terms, we have performed ablation studies by disabling each difference operator term, i.e., the spatial vertical difference term ($\|\mathcal{B} \times_1 \mathbf{D}_1\|_1$), spatial horizontal difference term ($\|\mathcal{G}^{(2)} \times_2 \mathbf{D}_2\|_1$), and spectral difference term ($\|\mathcal{G}^{(3)} \times_2 \mathbf{D}_3\|_1$), which are referred as w/o $\mathbf{D}_1$, w/o $\mathbf{D}_2$, and w/o $\mathbf{D}_3$, respectively. Table II lists the average quantitative results of ablation studies on the Pavia dataset. It is observed that the three different difference operators contribute to the performance of the proposed method.

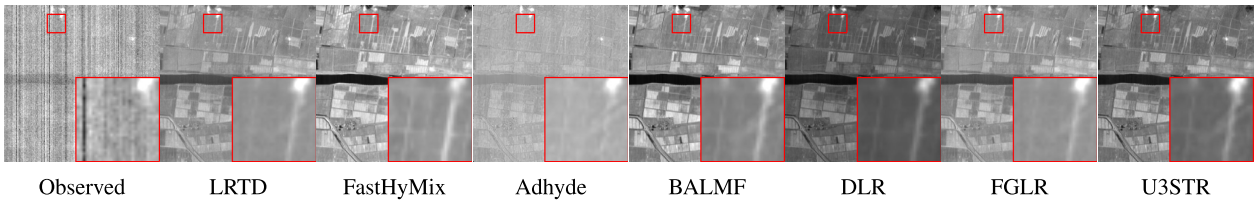


Fig. 3. Restored results of different methods on band 152 of the real GF-5 dataset.

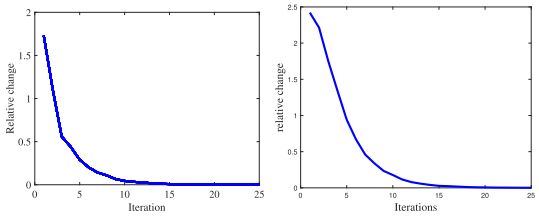


(a) (b)

Fig. 4. Relative change values of the image component versus the iteration number on the simulated Pavia and WDC datasets. (a) Pavia. (b) WDC.

*2) Numerical Convergence:* Fig. 4 displays the relative change value of the image component of our method on the simulated Pavia and WDC datasets under Case 1-1. We can observe that the relative change value converges to zero with the iteration increases, indicating the numerical convergence guarantee of our method.

## V. Conclusion

In this letter, we proposed a novel method called U3STR for HSI denoising and destriping. This method is highly effective in eliminating mixed noise, especially those of high intensity and dense stripe noise. The potent TR decomposition is employed to approximate the HSI, allowing the spatial information of HSI to be transferred to its TR factors. By encoding the local smoothness of TR factors, the global spatial–spectral correlation and local spatial–spectral smoothness of HSI are fully considered. The application of the ADMM algorithm guarantees an effective optimization to the proposed U3STR model. A series of simulated and real data experiments demonstrate the superior performance of our method over other advanced HSI denoising and destriping approaches, as evidenced by both visual and quantitative evaluations.

## References

[1] J. Li, W. He, W. Cao, L. Zhang, and H. Zhang, "UaNet: An uncertainty-aware network for building extraction from remote sensing images," *IEEE Trans. Geosci. Remote. Sens.*, vol. 62, pp. 1–13, 2024.

[2] L. Fang, G. Liu, S. Li, P. Ghamisi, and J. A. Benediktsson, "Hyperspectral image classification with squeeze multibias network," *IEEE Trans. Geosci. Remote Sens.*, vol. 57, no. 3, pp. 1291–1301, Mar. 2019.

[3] Y. Chang, L. Yan, and W. Liao, "HSI-DeNet: Hyperspectral image restoration via convolutional neural network," *IEEE Trans. Geosci. Remote Sens.*, vol. 57, no. 2, pp. 667–682, Feb. 2018.

[4] M. Li, J. Liu, Y. Fu, Y. Zhang, and D. Dou, "Spectral enhanced rectangle transformer for hyperspectral image denoising," in *Proc. IEEE Conf. Comput. Vis. Pattern Recognit. (CVPR)*, Apr. 2023, pp. 5805–5814.

[5] H. Zhang, W. He, L. Zhang, H. Shen, and Q. Yuan, "Hyperspectral image restoration using low-rank matrix recovery," *IEEE Trans. Geosci. Remote Sens.*, vol. 52, no. 8, pp. 4729–4743, Aug. 2013.

[6] Y. Chen, T. Huang, and X. Zhao, "Destriping of multispectral remote sensing image using low-rank tensor decomposition," *IEEE J. Sel. Topics Appl. Earth Observ. Remote Sens.*, vol. 11, no. 12, pp. 4950–4967, Dec. 2018.

[7] Y. Chen, X. Gui, J. Zeng, X.-L. Zhao, and W. He, "Combining low-rank and deep plug-and-play priors for snapshot compressive imaging," *IEEE Trans. Neural Netw. Learn. Syst.*, pp. 1–13, 2023.

[8] L. Zhuang and M. K. Ng, "FastHyMix: Fast and parameter-free hyperspectral image mixed noise removal," *IEEE Trans. Neural Netw. Learn. Syst.*, vol. 34, no. 8, pp. 4702–4716, Aug. 2023.

[9] S. Xu, X. Cao, J. Peng, Q. Ke, C. Ma, and D. Meng, "Hyperspectral image denoising by asymmetric noise modeling," *IEEE Trans. Geosci. Remote Sens.*, vol. 60, pp. 1–14, 2022.

[10] L. Zhuang, M. K. Ng, L. Gao, and Z. Wang, "Eigen-CNN: Eigenimages plus eigennoise level maps guided network for hyperspectral image denoising," *IEEE Trans. Geosci. Remote Sens.*, vol. 62, pp. 1–18, 2024, Art. no. 5512018, doi: 10.1109/TGRS.2024.3379199.

[11] Y. Chen, W. Lai, W. He, X.-L. Zhao, and J. Zeng, "Hyperspectral compressive snapshot reconstruction via coupled low-rank subspace representation and self-supervised deep network," *IEEE Trans. Image Process.*, vol. 33, pp. 926–941, 2024.

[12] W. He, H. Zhang, L. Zhang, and H. Shen, "Total-variation-regularized low-rank matrix factorization for hyperspectral image restoration," *IEEE Trans. Geosci. Remote Sens.*, vol. 54, no. 1, pp. 178–188, Jan. 2015.

[13] Y. Wang, J. Peng, Q. Zhao, Y. Leung, X.-L. Zhao, and D. Meng, "Hyperspectral image restoration via total variation regularized low-rank tensor decomposition," *IEEE J. Sel. Topics Appl. Earth Observ. Remote Sens.*, vol. 11, no. 4, pp. 1227–1243, Apr. 2018.

[14] Y. Chen, W. He, N. Yokoya, and T.-Z. Huang, "Hyperspectral image restoration using weighted group sparsity-regularized low-rank tensor decomposition," *IEEE Trans. Cybern.*, vol. 50, no. 8, pp. 3556–3570, Aug. 2020.

[15] J. Peng et al., "Fast noise removal in hyperspectral images via representative coefficient total variation," *IEEE Trans. Geosci. Remote Sens.*, vol. 60, pp. 1–17, 2022.

[16] Q. Xie, Q. Zhao, D. Meng, and Z. Xu, "Kronecker-basis-representation based tensor sparsity and its applications to tensor recovery," *IEEE Trans. Pattern Anal. Mach. Intell.*, vol. 40, no. 8, pp. 1888–1902, Aug. 2018.

[17] W. He et al., "Non-local meets global: An iterative paradigm for hyperspectral image restoration," *IEEE Trans. Pattern Anal. Mach. Intell.*, vol. 44, no. 4, pp. 2089–2107, Apr. 2022.

[18] T.-X. Jiang, L. Zhuang, T.-Z. Huang, X.-L. Zhao, and J. M. Bioucas-Dias, "Adaptive hyperspectral mixed noise removal," *IEEE Trans. Geosci. Remote Sens.*, vol. 60, pp. 1–13, 2022.

[19] H. Zhang, J. Cai, W. He, H. Shen, and L. Zhang, "Double low-rank matrix decomposition for hyperspectral image denoising and destriping," *IEEE Trans. Geosci. Remote Sens.*, vol. 60, pp. 1–19, 2022.

[20] X. Su, Z. Zhang, and F. Yang, "Fast hyperspectral image denoising and destriping method based on graph Laplacian regularization," *IEEE Trans. Geosci. Remote Sens.*, vol. 61, pp. 1–14, 2023.

[21] Q. Zhao, G. Zhou, S. Xie, L. Zhang, and A. Cichocki, "Tensor ring decomposition," 2016, *arXiv:1606.05535*.

[22] W. He, N. Yokoya, L. Yuan, and Q. Zhao, "Remote sensing image reconstruction using tensor ring completion and total variation," *IEEE Trans. Geosci. Remote Sens.*, vol. 57, no. 11, pp. 8998–9009, Nov. 2019.

[23] Y. Chen, J. Zeng, W. He, X.-L. Zhao, and T.-Z. Huang, "Hyperspectral and multispectral image fusion using factor smoothed tensor ring decomposition," *IEEE Trans. Geosci. Remote Sens.*, vol. 60, 2022, Art. no. 5515417.

[24] Y. Wang, W. Yin, and J. Zeng, "Global convergence of ADMM in nonconvex nonsmooth optimization," *J. Sci. Comput.*, vol. 78, pp. 29–63, Jun. 2015.